Hypo-viscoelastic modelling of in-plane shear in UD thermoset prepregs

Yi Wang[1*], Jonathan P.-H. Belnoue[1], Dmitry S. Ivanov[1] and Stephen R. Hallett[1]

[1]Bristol Composites Institute (ACCIS), University of Bristol, UK

*Corresponding Author: yi.wang@bristol.ac.uk

ABSTRACT

In-plane shear of prepreg material is one of the key deformation modes that affects defect generation in composites manufacturing processes such as Automated Fibre Placement (AFP) and Thermoforming. Recent characterisation of the evolution of uncured prepreg in-plane shear behaviour during manufacturing has revealed a strong influence of deformation rate and temperature on the measured response. In the present contribution, a phenomenological viscoelastic model for the observed behaviour is formulated using rate constitutive equations. Each of the components is related to an assumed micro-mechanical phenomenon (e.g. friction between the fibres, tensile loading of the fibres, etc). The proposed model is implemented into a user material subroutine for the Finite Element (FE) package Abaqus/Explicit. Model validation is performed by modelling experiments with loading programmes distinctly different from those used for material parameter extraction and it is concluded that state-of-the-art numerical models for AFP need to better represent in-plane shear.

Keywords: *Composite manufacturing; In-plane shear; Numerical modelling; Defect prediction*

1. INTRODUCTION

In the past decade, the progressive introduction of regulations aiming at reducing carbon dioxide emissions has triggered a growing demand for more sustainable transportation and renewable energy sources, fuelling an unprecedented use of high stiffness and light composite materials across the aerospace, automotive and renewable energy sectors. As a result, increased production rates and efficiency together with improved part quality and manufacturing consistency have become paramount. Considerable effort has therefore been dedicated to developing automated manufacturing processes of these materials. One of the mainstream advanced manufacturing techniques of composites structures is Automated Fibre Placement (AFP) [1]. The method is much more efficient for large components than traditional hand-layup. It helps reduce waste and allows greater design freedom through tow steering [2]. However, some key limitations of this technique, like the generation of imperfections and defects within the structure during the manufacturing process [3], requires a better understanding of generation mechanism and more reliable prediction capability to avoid their occurrence.

AFP is a development of Automated Tape Layup (ATL) [4] where 1/8 to 1/2-inch wide tows of prepreg materials (i.e. carbon or glass fibres pre-impregnated with thermoset or thermoplastic resin) are fed into a Computer Numerical Control (CNC) machine head and deposited on a mould. Up to 32 tows can be operated concurrently with a maximum linear speed of $1\ \mathrm{m.\,s^{-1}}$. Each tow can be cut and restarted separately. The prepreg deposition and adhesion is favoured by applying pressure on the material through a compaction roller and locally increasing the tackiness of the resin by heating the material with a lamp attached to the deposition head. One of the shortfalls of the technique is that it is prone to induce defects (such as wrinkles, or tape pull up) within a part, as finding the right combination of deposition parameters (i.e. lay-up speed, the compaction force, temperature of the lamp etc) is a complex task. Defects are particularly likely to form when prepreg tapes are steered to align the fibres with the geodesic path of doubly-curved moulds [1]. In such a case, or when the machine head path is curved, the mismatch between the inner and outer length of the prepreg tape results in the formation of out-of-plane wrinkles. Generally, the smaller the deposition radius, the more serious the defect. In industry, a notion of "critical radius" describes the minimum radius allowed during deposition. As defects can be responsible for as much as 36% knockdown of the part mechanical performances [5,6], they should be avoided when possible.

Classically, the critical radius is determined through long and expensive trial-and-error experimental campaigns. As pointed out by Poursartip [7], product design and manufacture can account for up to 70% of the total cost of a part. Numerical modelling of the process could help greatly reduce these costs by helping to conduct many of the initial trials virtually. Due to the complexity of the process (as briefly described above, the process is multi-physics, multiscale and involves many interactions between different bodies), most of the early work on predictive tools for defects generated in AFP have been analytical. Beakou et al. [8] proposed an approach where the deposited tape was modelled as an anisotropic thin plate resting on an elastic foundation, imitating the interaction between the tape and the tool. A closed form solution of the plate buckling problem and predictions for the critical radius were obtained using a Ritz method. The results were qualitatively assessed by contrasting the model predictions with experimental data. The approach was further developed by Matveev et al. [9] for dry fibres AFP and Belhaj et al. [10] who added a shear layer between the plate and the elastic foundation. The analytical approaches are computationally very efficient, however, their predictive capabilities are hindered by the many assumption made in the process of formulating an analytical expression for the process. Hence, many important aspects of AFP deposition such as the lay-up speed, the interactions between the AFP roller, etc cannot be taken into account. The viscoelastic properties of the prepreg tape (although viscoelastic foundation of previously deposited layers was considered in [11]), is generally ignored.

The acknowledgment of the limitations of analytical modelling (together with the growth of computational power) has triggered recent development of numerical models for AFP using the finite element (FE) method. Two research centres have grown the field in recent years: The Chair of Carbon Composites at the Technical University of Munich (TUM) [12–15] and the Concordia Centre for Composites (CONCOM)[11,16,17]. The frameworks developed at the two institutions are similar in that they both take account of every constituent involved (i.e. the roller, the prepreg and the tool plate), their interactions and the dynamic nature of the process. TUM work aimed at capturing the thermal history during the complete layup process. They developed user-subroutines in a commercially available FE package, i.e. a sequentially coupled thermo-mechanical framework where the all the heat exchange phenomenon (lamp radiation, prepreg conductance etc) were accounted for. The mechanical behaviour and interactions of each constituent of the set-up were, however, only approximately modelled, with the prepreg assumed to be linear elastic (with no variation of its properties with temperature) and the contact between the different bodies only preventing penetration and assumed to be frictionless. CONCOM, on the other hand, focused on the mechanical aspects of the problem while making the assumption that the process is isothermal (a temperature of 40°C at the nip point was assumed). A 3D mechanical model for the AFP deposition process was developed in Abaqus/Explicit. A linear response was assumed for the prepreg in longitudinal and in-plane shear. The tack properties of the interface between the prepreg and the aluminium mould was characterised and modelled by a probe tack test and a bilinear cohesive zone modelling approach respectively. The study showed that the model qualitatively predicted the occurrence of wrinkles and demonstrated the importance of tack properties in the wrinkle formation mechanism.

The forming of fibrous reinforcements (whether they are dry or pre-impregnated with resin) is a composite manufacturing process that is much better understood than AFP [18,19]. The field has generated a great deal of knowledge on dry fabrics and prepregs mechanics. Hence, it is well accepted that shearing is the main deformation mechanisms for biaxial fabrics and shear properties are critical in describing wrinkle formation adequately [20]. In the case of biaxial textile reinforcements, trellis shear (i.e. pure shear) is a natural deformation mode. Early in the forming process, the material is very compliant to shearing; as the deformation grows, the material becomes stiffer as more fibres (internally) engage in contact; eventually, the fabric becomes so stiff that out-of-plane buckling is energetically more favourable and wrinkles form [21]. The mechanics of UD reinforcements is different, i.e. it can be expected that sliding of fibres within the UD tape is not accompanied by the stiffening as the fabric as the deformation grows. However, the principle that the deformation mode that costs the least energy to the system dominates remains. AFP tape steering holds many similarities with forming in that it consists in forcing the material to conform to a shape that is different from its original geometry (which introduces distortions and residual stresses in the tape). On that respect, it is

interesting to note that even though both Beakou [8] and Matveev's [9] analytical expressions include a component accounting for tape shearing, state-of -the-art numerical models for AFP do not typically account for it.

Recent work [22] on characterisation of UD prepreg using a 10° off-axis tensile test, revealed a high dependency of the stresses generated by in-plane shearing of the tape on temperature and rate of deformation. In the present contribution, the paper studies the implications of variation in shear response on wrinkle formation mechanisms using numerical modelling. The first part of the manuscript briefly reviews the experimental results of [22]. After noticing that traditional models, where the shear response is assumed to be dominated by the inter-fibre resin flow, fail to capture the material's visco-elastic behaviour, a phenomenological model (based on a system of springs and dashpots in series and parallel) is proposed. Each constitutive element of the proposed model is related to an assumed physical phenomenon at the meso- and micro-scale. Then, the model is formulated in a hypo-viscoelastic framework and implemented in the commercial FE package Abaqus/Explicit as a user-defined VUMAT material subroutine. Comparisons between numerical and experimental results are conducted. The model is further validated by comparing its output to new experimental data obtained from a distinct loading trajectory, i.e. ramp-dwell tensile tests performed on prepreg tapes with fibres oriented at 10° from the main loading direction. Finally, numerical models of tapes subjected to in-plane bending illustrate how different assumed/modelled shear behaviours, related to different processing conditions (i.e. temperature and loading rate), result in different wrinkle patterns. Beyond AFP deposition, the proposed material characterisation method and modelling approach could also find applications to other composite manufacturing techniques such as thermoforming.

2. RHEOLOGY OF UD PREPREG SUBJECTED TO LONGITUDINAL SHEAR

2.1 Experimental results

Recent work on the experimental characterisation of in-plane shear in UD prepreg [22] has revealed large differences in tape behaviour at the range of temperature and deformation rates typical for processing conditions. In that publication, Wang et al. studied the influence of parameters such tape width, thickness, lay-up speed and processing temperature using a 10° off-axis test. A schematic of the test is shown in Figure 1. The geometry of the sample is characterised by the existence of a shear band area where the fibres are not clamped at either end. The test data reduction procedure relies on the assumption that the totality of the energy provided to the sample is dissipated in this region where the vast majority of the deformation occurs. Tests were conducted on a Shimadzu universal testing machine equipped with a thermal chamber. The load cell was 1 kN with a ±0.5% accuracy and the temperature in the chamber varied from 20°C to 100°C with 0.1°C accuracy. An La Vison 5MP Digital Image Correlation (DIC) system was used to obtain the shear strain field

in the samples and measure the onset of out of plane deformation (i.e. point in time from which all collected data must be disregarded as the sample does not deform only through shear anymore). LED strip lights were used to illuminate the interior of the chamber and reduce the issue of light reflection from the glass viewing window. The influence of the dimensions, test rates (0.001/s, 0.01 /s, 0.1/s) and temperatures (25°C / 50°C / 75°C) were systematically studied.

The prepreg system IM7-8552 from Hexcel® (which is a commonly used aerospace grade commercial carbon-epoxy systems) was used. Some of the obtained test results are recalled in Figure 2 and Figure 3. The shear stress-strain curves presented were plotted using the average strain measured in the localisation band and resolving the stress by separating the load applied on the sample into a shear and transverse tensile components. To illustrate the influence of the test rate curves measured at 25°C are displayed (Figure 2a). The same trend is observed for the other 2 temperatures. Similarly, Figure 2b presents data collected at a shear rate of 0.1 s^{-1} to show the effect of temperature on the measured behaviour. The range over which the data vary from one test repeat to another is represented by the shaded area surrounding the representative curves of each test condition. In addition to the large effect of temperature and test rates that has already been mentioned, the data also revealed that the apparent shear modulus (i.e. slope of the initially linear behaviour of the curves) of the material is rate-dependent (see Figure 3). The experiments provide foundation data for the numerical modelling work presented here and the approach is further used for validation tests by applying different loading scenarios.

2.2 **Analytical models**

The literature on the modelling of shear in resin melts reinforced with UD fibrous reinforcements is extensive. The main body of the work has consisted of trying to relate the measured behaviour, at the ply scale, to microstructural geometrical characteristics (e.g. fibre volume fraction, fibre radius etc) and physical-chemical composition (e.g. resin viscosity). These studies are based on the consideration of an elementary representative volume (unit cell) and fibres are represented as rigid entities obstructing the flow of resin. Contributions in the field include Rogers [23], Christensen [24], Binding [25], Coffin et al. [26], Pipes [27], Hjellming et al. [28] and Harrison et al. [29]. In a detailed review, Wang et.al [30] pointed out that these rheological models work reasonably well at low volume fraction but cannot predict accurately the viscosities (both transverse and longitudinal) of fibre reinforced melts at volume fraction greater than 0.5 (which is the case for aerospace grade materials). This is usually explained by the fact that these models essentially assume that prepreg behaves in a purely viscous manner. On the other hand, at high volume fraction, fibre to fibre contacts and load transfer between the resin and the fibres (due to higher drag force) are more likely and this will activate some elastic and/or friction contribution from the fibres

that the flow models do not account for. These assumptions have recently been given more credibility by Deignan et al. [31] who have shown, through FE modelling of the melt microstructure, that the introduction of these phenomena into the models helps to qualitatively capture the same trends as those observed experimentally. Another important point emerging from that study was that, at low speed, fibre friction dominates; whilst, for high deformation rate, viscous drag is responsible for most of the stresses generated in the material. In the latter case, the smaller the inter-fibre channel (i.e. the higher the volume fraction), the higher the apparent viscosity of the melt.

In Figure 4, the experimental data from Wang et al. [22] at the 3 test temperatures are compared with predictions made using the Christensen model [24] that was chosen for this comparison as it is the most widely adopted micro-mechanical model of fibre reinforced resin melts. The volume fraction of the IM7-8552 prepreg was assumed to be 0.5. The general expression of Christensen model is shown in Eq. (1).

$$\frac{\eta_{12}}{\eta_m} = \frac{1 + \alpha\hat{c}}{(1 - \beta\hat{c})^{1/2}(1 - \hat{c})^{1/2}} \tag{1}$$

where

$$\hat{c} = c/c_m$$

c and c_m are fibre volume fraction and the maximum packing fraction respectively ($c_m = \pi/2\sqrt{3}$ for hexagonal arrangement of fibres). α and β are two parameters related to c_m (here α and β are calculated to be 0.873 and 0.8815) [24].

The model performs poorly at capturing the experimental trends from the off-axis test. Generally, better agreement is obtained at higher temperatures (see Figure 4c) than at lower temperatures, where the resin has a high viscosity (Figure 4a) and may display some non-rate-dependent effects. As nothing accounts for it in the modelling assumptions, the experimentally observed variation of stresses with strain (i.e. elasticity) is not captured.

3. HYPO-VISCOELASTIC FRAMEWORK FOR PREPREG MODELLING

3.1 UD prepreg in-plane shear constitutive relation

Given the difficulties in generating a model for prepreg shear from first principles highlighted in the previous section, a more pragmatic approach is followed here. First, classical viscoelastic models [33,34], derived as combinations of springs and dashpots in series and parallel are used to fit the data. It is found that a slightly modified version of the Zener model [35] gives a good representation of the experimental data from Wang et al. [22]. The different components of the model are, then, associated to one of the assumed physical

micro-mechanisms. It is believed that the present contribution is a good intermediate step towards the formulation of an accurate physically-based model for prepreg shear.

Here, one of the two most simple viscoelastic models, the Kelvin-Voigt model [36] is used. It consists of a dashpot (viscous part) and a spring (elastic part) combined in parallel (see Figure 5a). The overall stress is the sum of the contributions from the two elements. The constitutive equation obtained from the model is expressed by:

$$\tau = G\gamma + \eta\dot{\gamma} \tag{2}$$

where G and η are the shear modulus and viscosity respectively. τ and γ are the shear stress and shear angle with $\dot{\gamma}$ being the shear angle rate. This model is able to fit the experimental data well (using the least square method). However, this leads to both the viscosity and the elastic modulus being dependent on the temperature and the deformation rate (as highlighted in Table 1). Whilst the rate-dependent viscosity is to be expected (see section 2.2), a rate-dependent elastic modulus, although consistent with the observations from Figure 3, is not physical.

Therefore, a new and more complex model has been proposed (see Figure 5b), whereby the spring from the Kelvin-Voigt model was replaced by a spring in series with a parallel combination of another spring and a dashpot (which introduces rate-dependency). The newly introduced system of springs and dashpots is governed by the stress/strain relations given in Eq. (3):

$$\begin{aligned} \tau_{total} = \tau_1 + \tau_2 \quad & \gamma_{total} = \gamma_1 = \gamma_2 \\ \tau_1 = \tau_{D_1} \quad & \gamma_1 = \gamma_{D_1} \\ \tau_2 = \tau_{S_1} = \tau_k \quad & \gamma_2 = \gamma_{S_1} + \gamma_k \\ \tau_k = \tau_{D_2} + \tau_{S_2} \quad & \gamma_k = \gamma_{D_2} = \gamma_{S_2} \end{aligned} \tag{3}$$

where the subscripts k, D_1, D_2, S_1, S_2 refer to Kelvin, dashpot one/two and spring one/ two, respectively. Rearranging Eq. (3) and replacing τ_i by their expressions ($\tau_{S_i} = G_i \cdot \gamma_i$ and $\tau_{D_i} = \eta_i \cdot \dot{\gamma}_i$) gives rise to the constitutive relation described in Eq. (4):

$$\frac{\eta_2}{G_1 + G_2} \cdot \dot{\tau} + \tau = \frac{G_1 G_2}{G_1 + G_2} \cdot \gamma + \left(\eta_1 + \frac{G_1 \eta_2}{G_1 + G_2}\right) \cdot \dot{\gamma} + \frac{\eta_1 \eta_2}{G_1 + G_2} \cdot \ddot{\gamma} \tag{4}$$

G_1 and G_2 are the shear moduli of spring 1 and 2 respectively. Similarly, η_1 and η_2 are the viscosity of the dashpots 1 and 2. γ and τ are the shear angle and shear stress of the proposed combination of springs and dashpots with $\dot{\gamma}$ and $\ddot{\gamma}$ the shear strain rate and its time derivative. In this work, it is assumed the value of $\ddot{\gamma}$ is very small and so can be ignored, based on the experimental observation that the shear rate is almost constant during the test [22]. An optimisation method, i.e. Generalized Reduced Gradient (GRG) Nonlinear approach, was used to fit model parameters to the corresponding experimental stress-strain curves of different

temperatures and shear rates. As illustrated in Figure 6, the model captures well the observed behaviour. The values extracted from the least-square fit of the experimental data for different temperatures and rates are reported in Table 2 and Table 3. As intended, constant, rate independent, values of the elastic constants at a given temperature are now obtained.

From a micro-mechanical perspective, η_1 is the apparent viscosity of the fibre reinforced viscous medium. As the viscosity of the resin, quite obviously, affects the behaviour of the system, this term is dependent on temperature (Table 2). Moreover, as reported in section 2.2, Deignan et al. [25] have shown that different deformation rates will result in different drag forces around the fibres and that this will, in turn, cause the viscosity of the melt to vary with applied rate. Based on these observations, it is not so surprising to see that η_1 also depends on the strain rate (see Table 2).

As hinted at when reporting our attempt to fit the experimental data with the Kelvin-Voigt model, the second part of the assembly is related to the loading of the fibres. The parallel assembly of spring (G_2) and dashpot (η_2) leads to a similar mathematical expression to the equation used to describe mixed lubrication in the relative sliding of prepreg plies during thermoforming [37]. η_2 naturally depends on temperature. but, counter-intuitively, that is also the case of G_2 (see Table 3). Further considerations of the micromechanical behaviour of prepreg reveals indeed the existence of frictional behaviour at the micro-scale. Unlike the simplifying assumptions in analytical models, fibres in prepreg are not perfectly straight [38] and show some slight waviness. This means that, at high volume fraction (i.e. > 0.5), the fibres are entangled, contacting each other at localised points or are very close to each other (i.e. only separated by a very thin layer of resin) at other locations. Moreover, in a similar way that temperature evolution changes the topology of the prepreg surface [37], it also leads to changes of the degree of impregnation and of the resin distribution within the prepreg. This, very likely, explains why G_2 varies with temperature. Finally, fibre contact and entanglement is responsible for the fibre bed to behave as a 3D network (i.e. with some resistance to loading and deformation) rather than separated individual entities "floating" within the viscous resin. The fibres' response to loading, characterised by the elastic constant G_1, is quite compliant as they mostly experience bending and torsion stresses and have very small radii (~ 3.5 μm for carbon fibres). Because the amount of relative slip of the fibres will control the magnitude of the fibre stresses, the elastic element, G_1, is combined in series with the mixed lubrication law. On the same note, it is interesting to remark that G_1 and η_2 are positively correlated with a linear regression coefficient of 0.995.

3.2 **Rate equations**

Hypo-elastic and hypo-viscoelastic laws (rate constitutive models) are one of the two commonly adopted approaches to describe the mechanical behaviour of dry or impregnated fibrous sheets using a 2D (two

dimensional) continuum mechanics approach [39,40], the other is the hyper-viscoelastic approach, as described in [41]. The hypo-elastic approach is particularly popular in the composite forming simulation area and is here extended to application of AFP tape shear. The main idea of the method is to capture the nonlinear behaviour of the material by small steps and relate the stress and strain at each increment. The general form of these laws is as follows:

$$\widehat{\boldsymbol{\sigma}}_{ij} = \boldsymbol{C} : \dot{\boldsymbol{\varepsilon}}_{ij} \tag{5}$$

where $\boldsymbol{\sigma}_{ij}$ and $\dot{\boldsymbol{\varepsilon}}_{ij}$ are the Eulerian Cauchy stress and strain rate tensor, respectively and $\boldsymbol{C}$ is the constitutive tensor used to define the behaviour of the material. As the derivative of $\boldsymbol{\sigma}_{ij}$ is not frame indifferent or objective (i.e. its invariants vary with the coordinate system chosen), Eq. (5) is expressed, instead, in terms of the objective stress rate, $\widehat{\boldsymbol{\sigma}}_{ij}$, which relates to $\boldsymbol{\sigma}_{ij}$ and the rigid body rotation, $\boldsymbol{Q}$, through Eq. (6).

$$\widehat{\boldsymbol{\sigma}}_{ij} = \boldsymbol{Q} \cdot \left[\frac{d}{dt} \left(\boldsymbol{Q}^T \cdot \boldsymbol{\sigma}_{ij} \cdot \boldsymbol{Q} \right) \right] \cdot \boldsymbol{Q}^T \tag{6}$$

Traditionally, FE implementations of objective stress rates use either the Green-Naghdi (G-N) or the Jaumann framework and $\boldsymbol{Q}$ is obtained based on polar or corotational frame rotation. However, as pointed out by Badel et al. [42], the material anisotropy and the presence of the fibres means that the rotation of the loading direction is different from that of the code work frame. As a result, $\widehat{\boldsymbol{\sigma}}_{ij}$ should be expressed with respect to fibres direction instead and the strain and stress tensors transformed accordingly.

As Abaqus/Explicit expects the stress to be calculated based on the G-N objective rate, procedures need to be implemented to rotate the different stress and strain quantities (and their respective rates) from the code work frame, $\{\boldsymbol{e}_i\}$, to the fibres frame $\{\boldsymbol{f}_i\}$ (see Figure 7) where $i = 1, 2$. By convention $\boldsymbol{f}_1$ is aligned with the fibres' direction (in the case of a fabric $\boldsymbol{f}_2$ would be aligned with the second fibre direction). After deformation, the code work and fibres frames can be expressed as:

$$\boldsymbol{e}_i = \boldsymbol{Q} \cdot \boldsymbol{e}_i^0 \tag{7}$$

and

$$\boldsymbol{f}_i = \frac{\boldsymbol{F} \cdot \boldsymbol{f}_i^0}{\left\| \boldsymbol{F} \cdot \boldsymbol{f}_i^0 \right\|} \tag{8}$$

where $\boldsymbol{e}_i^0$ and $\boldsymbol{f}_i^0$ are the initial direction vectors of the code work frame and the fibres frame respectively and $\boldsymbol{F}$ is the material's deformation gradient. $\boldsymbol{Q}$ is the rotation frame obtained through the polar decomposition of $\boldsymbol{F}$ expressed in Eq. (9).

$$\boldsymbol{F} = \boldsymbol{Q} \cdot \boldsymbol{U} \tag{9}$$

where $\boldsymbol{U}$ is the stretch tensor. User material subroutines for commercial FE software give both $\boldsymbol{F}$ and $\boldsymbol{U}$ at the start of each increment. Hence, $\boldsymbol{Q}$ can easily be computed from rearranging Eq. (9). In the G-N framework, the

angular velocity of corresponding rigid body rotation $\boldsymbol{\Omega} = \dot{\boldsymbol{Q}} \cdot \boldsymbol{Q}^{\boldsymbol{T}}$ is employed, hence the objective Cauchy stress derivative can be written:

$$\widehat{\boldsymbol{\sigma}}_{ij} = \dot{\boldsymbol{\sigma}} - \boldsymbol{\Omega} \cdot \boldsymbol{\sigma} - \boldsymbol{\sigma} \cdot \boldsymbol{\Omega}^{\boldsymbol{T}} \tag{10}$$

The angle between the fibre directions and the directions of the code work frame can be calculated as shown in Eq. (11) and the transformation matrix that links $\{\boldsymbol{e}_i\}$ to $\{\boldsymbol{f}_i\}$ directly follows from that as expressed in Eq. (12).

$$\theta_i = \arctan\left(\frac{\|\boldsymbol{e_i} \times \boldsymbol{f}_i\|}{\|\boldsymbol{e}_i \cdot \boldsymbol{f}_i\|}\right) \tag{11}$$

$$\boldsymbol{T}^{(\boldsymbol{i})} = \begin{bmatrix} cos\theta_i & -sin\theta_i \\ sin\theta_i & cos\theta_i \end{bmatrix} \tag{12}$$

The transformation matrices of Eq. (12) are then used to project (see Eq. (13)) the strain increment tensor onto each direction of the fibres frame $\{\boldsymbol{f}_i\}$ using the strain increment in the code work frame $\{\boldsymbol{e}_i\}$ (which would be provided to any user material subroutine for commercial FE codes).

$$d\boldsymbol{\varepsilon}_f{}^{(i)} = \boldsymbol{T}^{(\boldsymbol{i})} \cdot d\boldsymbol{\varepsilon}_e \cdot \boldsymbol{T}^{(\boldsymbol{i})^T} \tag{13}$$

Following this, the constitutive equations (Eq. (5)) can be applied to obtain the corresponding stress increment component associated with each direction of the fibres frame:

$$d\boldsymbol{\sigma}_f{}^{(i)} = \boldsymbol{C}_f \cdot d\boldsymbol{\varepsilon}_f{}^{(i)} \tag{14}$$

The stress state on each fibre direction at increment $n+1$ can then be derived by integrating Eq. (15) using a mid-point rule.

$$\boldsymbol{\sigma}^{n+1}{}_f{}^{(i)} = \boldsymbol{\sigma}^{n}{}_f{}^{(i)} + \boldsymbol{C}^{n+1/2}{}_f \cdot d\boldsymbol{\varepsilon}^{n+\frac{1}{2}}{}_f{}^{(i)} \tag{15}$$

The last step in the hypo-viscoelastic continuum description of fibrous materials is to rotate the stress tensors associated with each directions of the fibres frame back into the code work frame and assemble the total stress tensor of the material from the resulting tensors (see Eq. (16)).

$$\boldsymbol{\sigma}^{n+1} = \sum_{i=1}^{2} \boldsymbol{T}^{(\boldsymbol{i})^T} \cdot \boldsymbol{\sigma}^{n+1}{}_f{}^{(i)} \cdot \boldsymbol{T}^{(\boldsymbol{i})} \tag{16}$$

3.3 **Implementation and evolution with temperature and rate of the model parameters**

The shear model of section 3.1 was then implemented in the hypo-viscoelastic framework of section 3.2 as a Fortran user material subroutine (i.e. VUMAT) for the FE package Abaqus/Explicit. The initial fibre direction and the Young's moduli in the directions defining the fibre frame (E_1 and E_2 respectively) were given as inputs to the subroutine. Instead of using the more compact tensorial calculus formulation of Eq. (14), each component of the stress rate tensor is updated one by one as shown in Eq. (17) and (18) (where Eq. (18) is

derived from Eq. (4)). The relation between the tensorial shear strain and engineering strain $\gamma = 2\varepsilon_{12}$ was considered.

$$\Delta\sigma_{jj_f}{}^{(i)} = E_j \cdot \Delta\varepsilon_{jj_f}{}^{(i)} \text{ with } j = 1, 2 \tag{17}$$

$$\Delta\tau_{12_f}{}^{(i)} = \frac{1}{1 + \frac{\eta_2}{(G_1 + G_2)\Delta t}} \cdot \left(\frac{G_1 G_2}{G_1 + G_2} \cdot \left(\varepsilon_{12}{}^{n}{}_f{}^{(i)} + \Delta\varepsilon_{12_f}{}^{(i)} \right) + \left(\eta_1 + \frac{G_1}{G_1 + G_2} \right) \cdot \frac{\Delta\varepsilon_{12_f}{}^{(i)}}{\Delta t} - \tau_{12}{}^{n}{}_f{}^{(i)} \right) \tag{18}$$

In the subroutine code, deformation in the fibres' direction and its transverse are assumed to be elastic. Shear, on the other hand, is dependent on the loading rate and temperature. This assumption is reasonable on the basis that: 1) in the fibres' direction the high elastic stiffness will generate stresses that are much higher than those created by any (resin dominated) viscous behaviour and 2) that, although, the transverse direction is strongly dominated by the resin, the mechanical behaviour in that direction is so compliant that it only marginally contributes to the energy dissipated by the material. In the model, $E_1 = 10{,}000\ MPa$ [43] and $E_2 = 1\ MPa$ were used.

The physical meaning of the other parameters (that control the shear response of the material) has been discussed, at length, in section 3.1 where it was also mentioned that G_1, G_2 and η_2 vary with temperature whilst η_1 depends on both temperature and loading rate. Values for these parameters at fixed test rates (i.e. 0.001/s, 0.01 /s and 0.1/s) and temperatures (i.e. 25°C, 50°C and 75°C) were provided. Generalisation of the model to any temperature and test rates and variation of these two quantities would normally be performed by simply assuming piecewise linear variation in the processing parameter space. However, as the testing and data extraction procedure is quite time consuming, relatively few experimental data points are available and it might be that a more complex fit of the data would be beneficial. This is reinforced by the very non-linear nature of the phenomena (i.e. the parameters vary more between 25°C and 50°C than between 50°C and 75°C as shown in Tables 2 and 3). As power-law functions are often used to describe the variation of resin viscosity with temperature [44] they also appear as a natural choice to represent the evolution of G_1, G_2 and η_2. Moreover, rate dependent material viscosity is often modelled using Carreau [45] rheological equations that combine a Newtonian behaviour (at low rate) with a power-law fluid. It is known that real fluids often display an even more complex behaviour where the fluid transitions from a Newtonian behaviour, at low rate, to another, at high rate, and behaves as a power law fluid between these 2 states. This sort of behaviour can be represented by using a tangent hyperbolic-based function [46]. This is the choice made here for the variation of η_1 with the applied strain rate. This necessitated the acquisition of extra test data as 4 parameters are needed and only 3 test rates were considered in the original test program. The same method as in the previous experimental work [25] was used. A (very low) test rate of $1e^{-12}$/s was used which led to each test taking over 4 hours to complete. One

test repeat was performed at each of the temperatures (i.e. 25ºC, 50ºC and 75ºC) considered. The variation of η_1 with temperature was assumed linear. These considerations led to the expressions for G_1, G_2 and η_2 taking the form described by Eq. (19) (where K_I refers to the parameter G_1, G_2 and η_2, T is the temperature, α_i, n_i and β_i take different values for each of the parameters) and η_1 being described by Eq. (20) (where a_{T_i}, b_{T_i}, w_{T_i} and c_{T_i} are four temperature-dependent coefficients, $\dot{\gamma}$ is the shear rate).

$$K_\mathrm{I} = \alpha_i T^{n_i} + \beta_i \tag{19}$$

$$\eta_2 = \frac{a_{T_i}+b_{T_i}}{2} + \frac{a_{T_i}-b_{T_i}}{2} \times f_{T_i} \text{ with } f_{T_i} = \tanh\left(\frac{(log(\dot{\gamma})+c_{T_i})}{w_{T_i}/10}\right) \tag{20}$$

Fitting of the experimental data was done using Matlab®. This resulted in the parameter values reported in Table 4 and Table 5. Graphical representation of the obtained fits is provided in Figure 8.

4. MODEL VERIFICATION AND VALIDATION

4.1 FE model

For purpose of verification and checking the validity of the proposed approach, an FE model of the off-axis tensile test was built in ABAQUS/Explicit (Figure 9). The same sample geometry (i.e. size and thickness) as in the experiments was used. The multiple layers of the sample were simulated as one single thick layer. The boundary conditions were set to be consistent with the test setup with fully fixed nodes at one end and an applied displacement boundary condition in the y-direction at the other end, where all the other degrees of freedom were fixed. Continuum reduced integration triangular membrane elements (M3D3R), which do not consider the bending stiffness, were adopted. The material constitutive behaviour was completely defined by the VUMAT subroutine described in the previous section. The fibre direction (i.e. 10°) was given as an input to the code. All the test cases (three test rates at three different temperatures) were simulated. The related parameters for material behaviour characterisation were directly obtained from the experimental test, as discussed in sections 3.1 and 3.3. Mass scaling was not used. To decrease the simulation CPU time, a pseudo-time, i.e. real time/1000, is adopted and this is accounted for by multiplying the simulation time by 1000 in the VUMAT for time dependent parameters. The same data reduction procedure as per the experiments was used. Hence, the evolution, with time, of the shear strains were extracted from all the elements within the shear band and averaged; and the shear stress was calculated from the load extracted in the FE model using the procedure described by Wang et al. [22]. These were used to plot stress vs strain evolution for each combination of temperature and loading rate considered.

4.2 Model verification

Figure 10 shows a representative shear strain field, experimentally obtained via Digital Image Correlation (DIC), and the corresponding FE prediction at 25°C and a test rate of 0.01/s. The model is shown to reproduce

the shear strain distribution observed in the experiments. The shear strain in the localisation band is, mostly, uniform and much higher than that of the surrounding areas. All the different cases show a similar degree of agreement to the one shown in the figure.

Quantitative assessment of the model was also conducted. Predicted shear stress-strain curves are compared in Figure 11 to those experimentally measured. Overall, there is a good match between the numerical predictions and the experimental data. It is, in particular, able to capture the rate and temperature dependent viscoelastic behaviour of the uncured prepreg. The "oscillations" appearing on 75°C curves are a result of numerical instability from the explicit solver. As these models only reproduce the tests form which the material parameters were extracted, it verifies that the model was properly implemented in the VUMAT subroutine but does not fully validate the approach.

4.3 **Model validation**

To validate the model, new specimens were manufactured and tested in a Shimadzu universal test machine with a temperature-controlled thermal chamber. The test procedure was the same as that described in section 2 but with an altered loading program. Displacement-control was applied. The ramp-dwell test program is illustrated in Figure 12 and aimed at showcasing the model's ability to operate within a fairly large range of loading rates and when the loading is non-monotonic. A displacement of 1.5 mm is first applied in 4 seconds and then held for 6 seconds. The machine cross head is then moved up a further 1.5 mm in 4 seconds. The shear deformation rates vary between 0 and 0.01/s (corresponding to the loading rate at the ramp stage) and the overall displacement is 3 mm. This was chosen based on the previous experiments that have shown that for a deformation rate of 0.01/s, significant out of plane wrinkles appear when the cross-head displacement is larger than 3 mm. The predictive capability of the model was assessed by conducting tests at 25°C (i.e. one of the temperatures at which the model parameters were extracted) and 40°C which is close to the nip point temperature in the AFP deposition process. For both cases five repeats were conducted to show the full extent of the test experimental variation. The test data were then processed according to [22] and compared with model predictions.

In Figure 13a shear stress vs test time curves obtained experimentally for the tests performed at 25°C are superimposed to predictions made using the FE model (see section 4.1) of the corresponding test conditions. The FE predictions fall very slightly outside the cloud representing the variation of the experimental data but overall follows the experimental data well. The model is able to capture the relaxation experimentally observed when the machine cross-head displacement is kept constant (i.e. the dwell) as well as all viscoelasticity-induced nonlinearities occurring when the samples are deformed at

constant rate. This essentially validates the fitting procedure of the experimentally extracted parameter η_1 that was described at length in section 3.3 and Figure 8.

Validation of the fitting procedure for parameters varying with temperature was performed, comparing the model output to experimental results collected from the tests performed at 40°C. Comparison between model predictions for the evolution of stress with time and corresponding experimental results is provided in Figure 13b. Again, the average and the error band of the five test results was calculated and plotted on the graph. At all stages of the loading program, the numerical predictions are within the error band of the experimental results which demonstrates the good predictive capabilities of the modelling approach described at length in section 3.

Finally, to illustrate the necessity of the non-linear fitting to the calibration data proposed in section 3.3, a last model was run whereby piecewise linear evolution of the parameters with both temperature and strain rate was assumed. The obtained evolution of stress with time is plotted in Figure 14 together with the corresponding experimental and nonlinear fit predicted curves already shown in Figure 13b. The results indicate that the value predicted by a linear interpolation function is much higher than that using the non-linear fitting of the experimental data. It was shown in Figure 8 (particularly for G_1) that the 2 types of interpolation of the experimental data resulted in very different estimation of the parameter values at 40°C and this certainly explains the differences observed here. This results clearly justifies the need for more complex fit of the data, as proposed in section 3.3.

5. HOW DOES SHEAR AFFECTS OUT-OF-PLANE DEFORMATION OF NARROW TAPES SUBJECTED TO IN-PLANE BENDING?

As was noted in the introduction, shear has not traditionally been considered as one of the major deformation mechanisms by which out-of-plane defects appear during the steering of tapes in the AFP deposition process. This is often justified by assuming that the fibres within a piece of prepreg are separated by a layer of resin and can almost freely slide with respect to another. However, the experiments from Wang et al. [22], have revealed that, as opposed to common assumptions, non-negligible stresses can be generated in prepreg sheets under shear deformation, especially at high deformation rate and low temperature. In addition, shear is well known to be a major factor that influences defect production when fibrous sheets are formed over doubly-curved surfaces and shear terms also appear in analytical expressions that estimate critical steering radius in AFP [9]. The present section investigates further how out-of-plane deformation of tapes subjected to in-plane bending is affected by the shear behaviour of the tape. It aims at assessing whether state-of-the-art predictive tools for AFP should improve the shear characterisation and modelling of the incoming material.

A numerical study is conducted using the FE software Abaqus/Explicit. As illustrated in Figure 15a, the model of a narrow tape of prepreg laying on a rigid substrate and subjected to in-plane bending was set-up. The tape dimensions were 6 mm × 50 mm × 0.15 mm with fixed displacement boundary conditions applied at one end of the tape and a displacement-controlled loading applied, in the y-direction, at the other end. The displacement in z-direction, is blocked, i.e. U3=0. A gravity load was also applied to initiate the (frictionless) contact between the tape and the substrate that was fixed. The tape was modelled by superimposed shell (S4R) and membrane (M3D4R) elements which has been demonstrated to be an good method to capture the decoupled in-plane (i.e. shear, fibre and transverse elongation) and out-of-plane (i.e. bending) behaviour characteristic of fibrous material [43]. In this approach, the membrane elements are used to describe the in-plane properties while the shell elements represent the out-of-plane behaviour of the material. The two element types were separately defined and then merged to combine the 2 behaviours, as illustrated in Figure 15b. A total of 896 elements were used in the model. In both element types, the VUMAT presented in section 3.3 was used. Elongation properties in the membrane elements were set to $E_1 = 150{,}000\ MPa$ and $E_2 = 1\ MPa$) with the membrane formulation having no bending properties. A low young's modulus of $E_1 = 100\ MPa$ was set in the shell elements to model bending behaviour, with the shear behaviour and transverse elongation properties were deactivated (modulus set to zero). It is worth noting here that, apart from those controlling the shear behaviour, all the material constants are independent of the loading and temperature conditions. Hence, any difference observed between the different cases will result from the variation of the shear behaviour alone.

Two different applied rates (i.e. 10 mm/s and 1mm/s) and two temperatures (i.e. 40°C and 60°C) which are consistent with the actual AFP deposition process were selected for this study. Out-of-plane wrinkles in prepreg tapes loaded under in-plane bending are traditionally explained by the fact that the inner radius of the tape is in compression and that out-of-plane deformation is energetically more favourable than compression of the material. Similar arguments can be made with respect to the shear response. Under conditions where the material's shear response is compliant (i.e. high temperature and low speed), out-of-plane wrinkles will occur at a later stage than at high deformation rate and high pressure when shear is energetically costly. This is confirmed by analysing the results from the different FE models run (see Figure 16). Tapes deformed at 10 mm/s display a significantly different wrinkle pattern (i.e. more wrinkles that are also shaper) and shear angle distribution than those loaded at 1 mm/s. Although, less pronounced, temperature also has an effect, as even if the shear distribution in the tape looks similar, the wrinkle amplitude and width are different. This can be related to the experimental measurements that showed that rate is the test parameter that influence the shear stress the most. Quantitative comparison of the wrinkles generated under the different conditions is provided in Table 6. These results highlight the significant influence of in-plane shear properties on tapes' out-of-plane

deformation and suggest the need for predictive tools of the AFP process to better account for the material shear behaviour.

6. CONCLUSION

This paper explores the modelling of in-plane shear of UD prepreg under processing conditions. Based on experimental results reported in a previous publication [23], a phenomenological model built from an assembly of springs and dashpots in series and parallel was proposed. Each constituent of the model was then associated with known micro-mechanical phenomena occurring when the material is deformed. In the authors views, this is only a first step towards a more comprehensive model for UD prepreg shear directly derived from first principles. The model parameters were extracted by an inverse method on the experimental data. Hypo-viscoelastic constitutive laws that include the proposed model were then derived and implemented as a user material subroutine (VUMAT) for the FE software Abaqus/Explicit. The model implementation was verified by comparing model predictions to the experimental measurements from which parameters were extracted. A new set of experiments with non-monotonic loading and performed at a temperature (i.e. 40°C) that is different from those at which the parameters were extracted was used to validate the model's predictive capabilities.

In the last section of the manuscript, the model is used to explore how the variations of prepreg shear behaviour with loading rate and temperature influence the out-of-plane-wrinkling of narrow tapes of prepreg subjected to in-plane bending. It is concluded, that in the context of composites automated manufacturing that uses AFP machines, state-of-the-art models of the process should account for the non-linear shear behaviour of the incoming material. This contribution lays the ground for a greater accuracy of digital twins of composite manufacturing and adds to the knowledge that can form the basis of a future strategy for virtual manufacturing of composites.

ACKNOWLEDGEMENT

This work was funded by the Engineering and Physical Sciences Research Council (EPSRC) through the Centre for Doctoral Training in Advanced Composites for Innovation and Science (grant no. EP/ L016028/1) and the platform grant "Simulation of new manufacturing Processes for Composite Structures (SIMPROCS)" (grant no. EP/ P027350/1). Yi Wang acknowledges the support from the China Scholarship Council.

REFERENCES

[1] Lukaszewicz DHJA, Ward C, Potter KD. The engineering aspects of automated prepreg layup: History, present and future. Compos Part B Eng 2012;43:997–1009.

[2] Stanford BK, Jutte C V., Chauncey Wu K. Aeroelastic benefits of tow steering for composite plates. Compos Struct 2014;118:416–22.

[3] Heinecke F, Willberg C. Manufacturing-Induced Imperfections in Composite Parts Manufactured via

Automated Fiber Placement. J Compos Sci 2019;3:56.

[4] Grimshaw MN, Grant CG, Diaz JML. Advanced technology tape laying for affordable manufacturing of large composite structures. Int SAMPE Symp Exhib 2001;46 II:2484–94.

[5] Ohare Adams D, Hyer MW. Analysis of layer waviness in flat compression-loaded thermoplastic composite laminates. J Eng Mater Technol Trans ASME 1996;118:63–70.

[6] Varkonyi B, Belnoue JPH, Kratz J, Hallett SR. Predicting consolidation-induced wrinkles and their effects on composites structural performance. Int J Mater Form 2019..

[7] Poursatip A. Transitioning Composites Manufacturing Simulation into Industrial Practice: Challenges and Opportunities. ICMAC 2015-International Conf. Manuf. Adv. Compos. Bristol, United Kingdom, 2015.

[8] Beakou A, Cano M, Le Cam JB, Verney V. Modelling slit tape buckling during automated prepreg manufacturing: A local approach. Compos Struct 2011;93:2628–35.

[9] Matveev MY, Schubel PJ, Long AC, Jones IA. Understanding the buckling behaviour of steered tows in Automated Dry Fibre Placement (ADFP). Compos Part A Appl Sci Manuf 2016;90:451–6.

[10] Belhaj M, Hojjati M. Wrinkle formation during steering in automated fiber placement: Modeling and experimental verification. J Reinf Plast Compos 2018;37:396–409.

[11] Bakhshi N, Hojjati M. Time-dependent wrinkle formation during tow steering in automated fiber placement. Compos Part B 2019;165:586–93.

[12] Lichtinger R, Hörmann P, Stelzl D, Hinterhölzl R. The effects of heat input on adjacent paths during Automated Fibre Placement. Compos Part A Appl Sci Manuf 2015;68:387–97.

[13] Lichtinger R, Lacalle J, Hinterhölzl R, Beier U, Drechsler K. Simulation and experimental validation of gaps and bridging in the automated fiber placement process. Sci Eng Compos Mater 2015;22:131–48.

[14] Kollmannsberger A, Lichtinger R, Hohenester F, Ebel C, Drechsler K. Numerical analysis of the temperature profile during the laser-assisted automated fiber placement of CFRP tapes with thermoplastic matrix. J Thermoplast Compos Mater 2018;31:1563–86.

[15] Hormann P. Thermoset automated fibre placement on steering effects and their prediction. Technical University of Munich, 2015. PhD thesis.

[16] Bakhshi N, Hojjati M. An experimental and simulative study on the defects appeared during tow steering in automated fiber placement. Compos Part A Appl Sci Manuf 2018;113:122–31.

[17] Bakhshi N, Hojjati M. Effect of compaction roller on layup quality and defects formation in automated fiber placement. J Reinf Plast Compos 2020;39:3–20.

[18] Akkerman R, Haanappel SP, Sachs U. History and future of composites forming analysis. IOP Conf Ser Mater Sci Eng 2018;406.

[19] Boisse P, Colmars J, Hamila N, Naouar N, Steer Q. Bending and wrinkling of composite fiber preforms and prepregs. A review and new developments in the draping simulations. Compos Part B Eng 2018;141:234–49.

[20] Syerko E, Comas-Cardona S, Binetruy C. Models for shear properties/behavior of dry fibrous materials at various scales: a review. Int J Mater Form 2015;8:1–23.

[21] Matveev MY, Endruweit A, De Focatiis DSA, Long AC, Warrior NA. A novel criterion for the prediction of meso-scale defects in textile preforming. Compos Struct 2019;226:111263.

[22] Wang Y, Chea MK, Belnoue JPH, Kratz J, Ivanov DS, Hallett SR. Experimental characterisation of the in-plane shear behaviour of UD thermoset prepregs under processing conditions. Compos Part A Appl Sci Manuf 2020;133:105865.

[23] Rogers TG. Squeezing flow of fibre-reinforced viscous fluids. J Eng Math 1989;23:81–9.

[24] Christensen RM. Effective viscous flow properties for fiber suspensions under concentrated conditions. J Rheol 1993;37:103–21.

[25] Binding DM. Capillary and contraction flow of long- (glass) fibre filled polypropylene. Compos Manuf 1991;2:243–52.

[26] Coffin DW, Pipes RB, Šimáček P. First-Order Approximations for the Effective Shearing Viscosities of Continuous-Fiber Suspensions. J Compos Mater 1995;29:1169–80.

[27] Pipes RB. Oriented Fiber Composite with Anisotropic a 2016;26:1536–52.

[28] Hjellming LN, Walker JS. Motion of Continuous Fibers through a Newtonian Resin for High Fiber Volume Fraction. J Compos Mater 1990;24:853–78.

[29] Harrison P, Clifford MJ, Long AC, Rudd CD. A constituent-based predictive approach to modelling the rheology of viscous textile composites. Compos Part A Appl Sci Manuf 2004;35:915–31.

[30] Wang J, Ge X, Liu Y, Qi Z, Li L, Sun S, et al. A review on theoretical modelling for shearing viscosities of continuous fibre-reinforced polymer composites. Rheol Acta 2019;58:321–31.

[31] Deignan A, Figiel, McCarthy MA. Insights into complex rheological behaviour of carbon fibre/PEEK from a novel numerical methodology incorporating fibre friction and melt viscosity. Compos Struct 2018;189:614–26.

[32] Habibi MH. Effects of out-time on cure kinetics and rheological properties of out-of-autoclave and autoclave prepregs. Wichita State University, 2013.

[33] Faal RT, Sourki R, Crawford B, Vaziri R, Milani AS. Using Fractional Derivatives for Improved

Viscoelastic Modeling of Textile Composites. Part II: Fabric under Different Temperatures. Compos Struct 2020;248:112494.

[34] Faal RT, Sourki R, Crawford B, Vaziri R, Milani AS. Using fractional derivatives for improved viscoelastic modeling of textile composites. Part I: Fabric yarns. J Compos Mater 2020.

[35] Roylance D. Engineering viscoelasticity. Dep Mater Sci Eng Inst Technol Cambridge MA 2001;2139:1–37.

[36] Larberg Y, Akermo M. In-plane deformation of multi-layered unidirectional thermoset prepreg - Modelling and experimental verification. Compos Part A Appl Sci Manuf 2014;56:203–12.

[37] Rashidi A, Montazerian H, Yesilcimen K, Milani AS. Experimental characterization of the inter-ply shear behavior of dry and prepreg woven fabrics: Significance of mixed lubrication mode during thermoset composites processing. Compos Part A Appl Sci Manuf 2020;129:105725.

[38] Gutowski TG, Cai Z, Bauer S, Boucher D, Kingery J, Wineman S. Consolidation Experiments for Laminate Composites. J Compos Mater 1987;21:650–69.

[39] Crisfield MA. Non-linear finite element analysis of solids and structures. vol. 1. Wiley New York; 1993.

[40] Belytschko T, Liu WK, Moran B, Elkhodary K. Nonlinear finite elements for continua and structures. John wiley & sons; 2013.

[41] Guzman-Maldonado E, Hamila N, Naouar N, Moulin G, Boisse P. Simulation of thermoplastic prepreg thermoforming based on a visco-hyperelastic model and a thermal homogenization. Mater Des 2016;93:431–42.

[42] Badel P, Vidal-Sallé E, Boisse P. Large deformation analysis of fibrous materials using rate constitutive equations. Comput Struct 2008;86:1164–75.

[43] Thompson AJ, Belnoue JPH, Hallett SR. Defect formation induced by the forming of multiple layers of 2D woven fabrics. Compos Part B 2020.

[44] Van Ee D, Poursartip A. NCAMP Hexply Material Properties Database for Use With COMPRO CCA and Raven. Natl Cent Adv Mater Perform (NCAMP), Wichita, KS 2009.

[45] Carreau PJ. Rheological Equations From Molecular Network Theories. Trans Soc Rheol 1972;16:99–127.

[46] Ivanov DS, Lomov S V. Compaction behaviour of dense sheared woven preforms: Experimental observations and analytical predictions. Compos Part A Appl Sci Manuf 2014;64:167–76.

Figures

(a) (b)

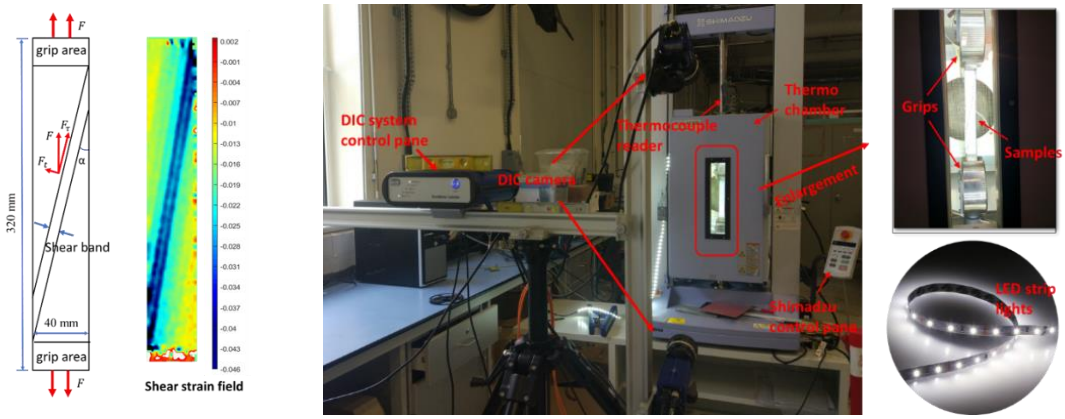

Figure 1 Schematic of the test: (a) Sample Dimensions and typical DIC results (b) Test set up [22].

(a) (b)

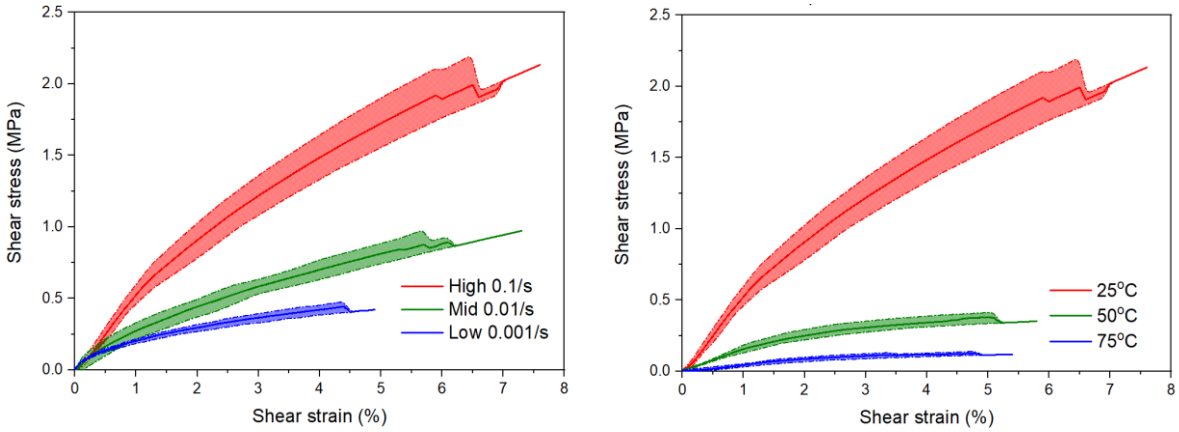

Figure 2 The evolution of the shear stress-strain curves of IM7-8552: (a) at 25°C with different test rates (b) at 0.1/s with different temperatures [22].

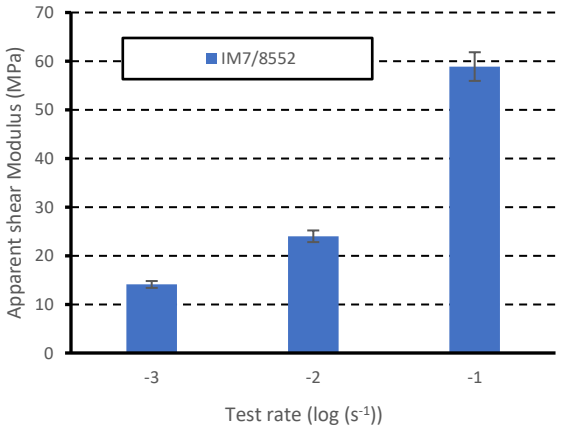

Figure 3 Variation of the apparent shear modulus with test rate at 25°C [22].

(a)

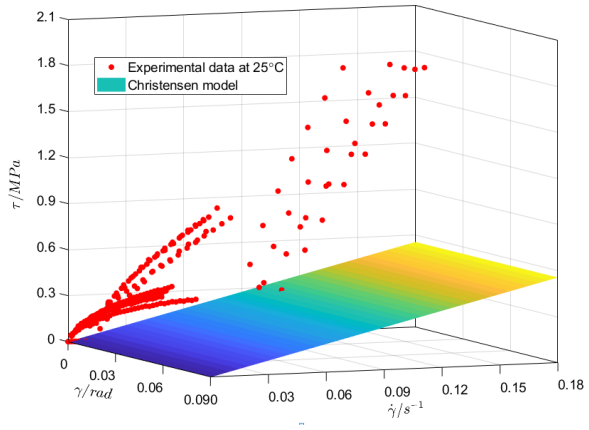

(b)

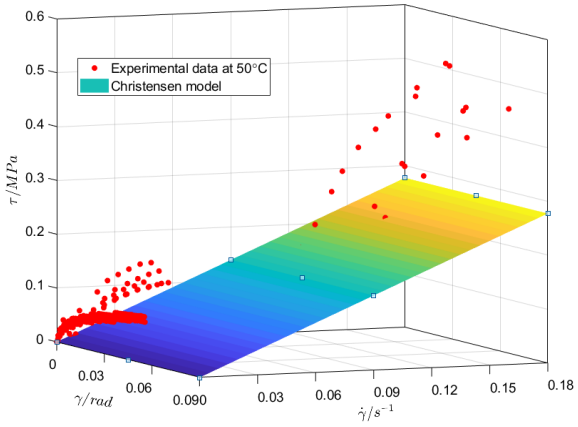

(c)

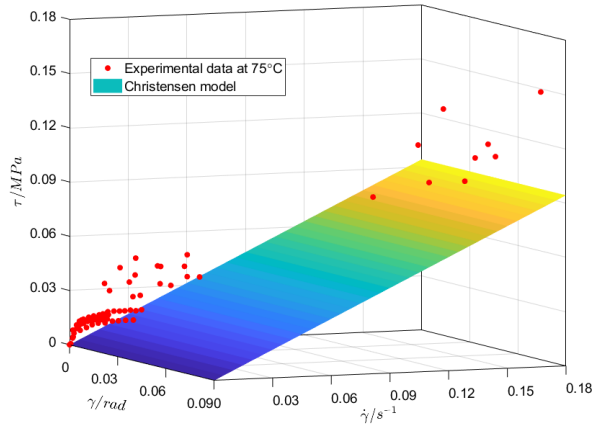

Figure 4 Comparison of the experimentally measured relation between stress, strain and strain rate with prediction made using the Christensen [24] *micro-mechanical model* at (a) 25°C, (b) 50°C and (c) 75°C. *Resin viscosities for epoxy resin 8552 used in Christensen expression were extracted from* [32].

(a) (b)

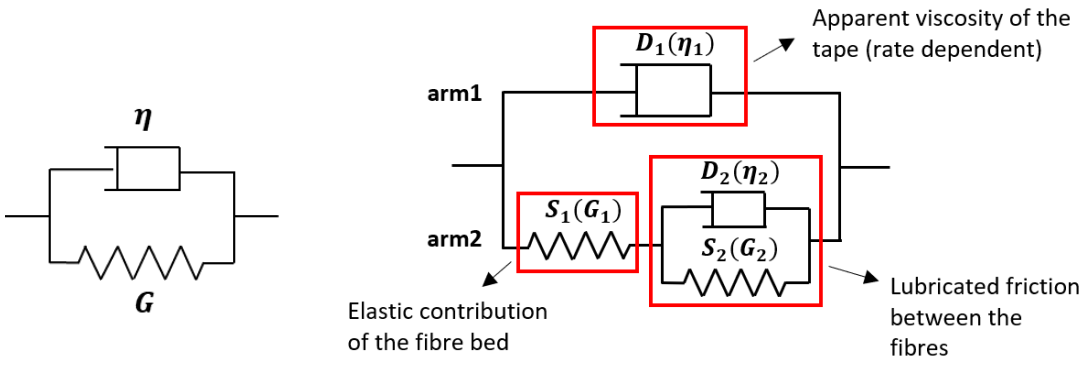

Figure 5 Kelvin-Voigt model and proposed nonlinear viscoelastic model.

(a) (b)

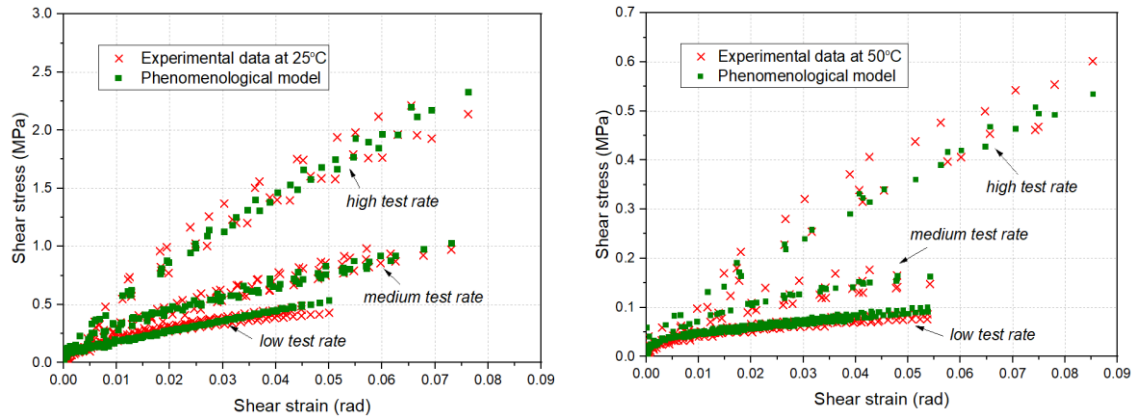

(c)

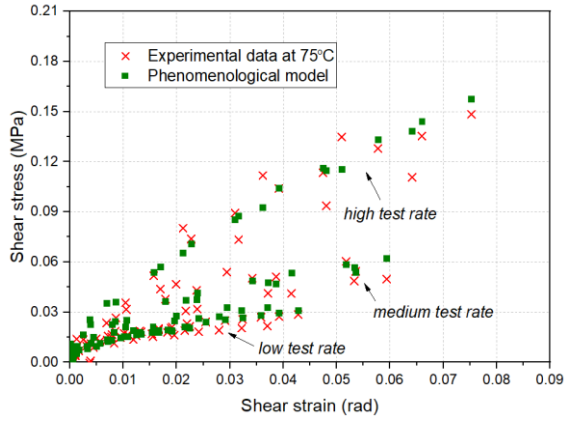

Figure 6 Model fit vs. Experiment results based on nonlinear viscoelastic model at (a) 25°C, (b) 50°C and (c) 75°C.

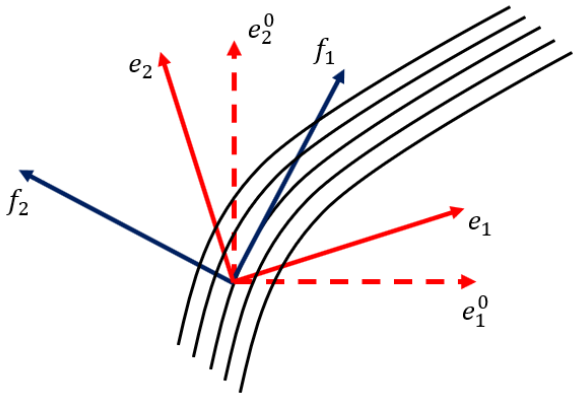

Figure 7 Initial code work frame $\{e_i^0\}$, rotated code work frame $\{e_i\}$ and fibre frame$\{f_i\}$.

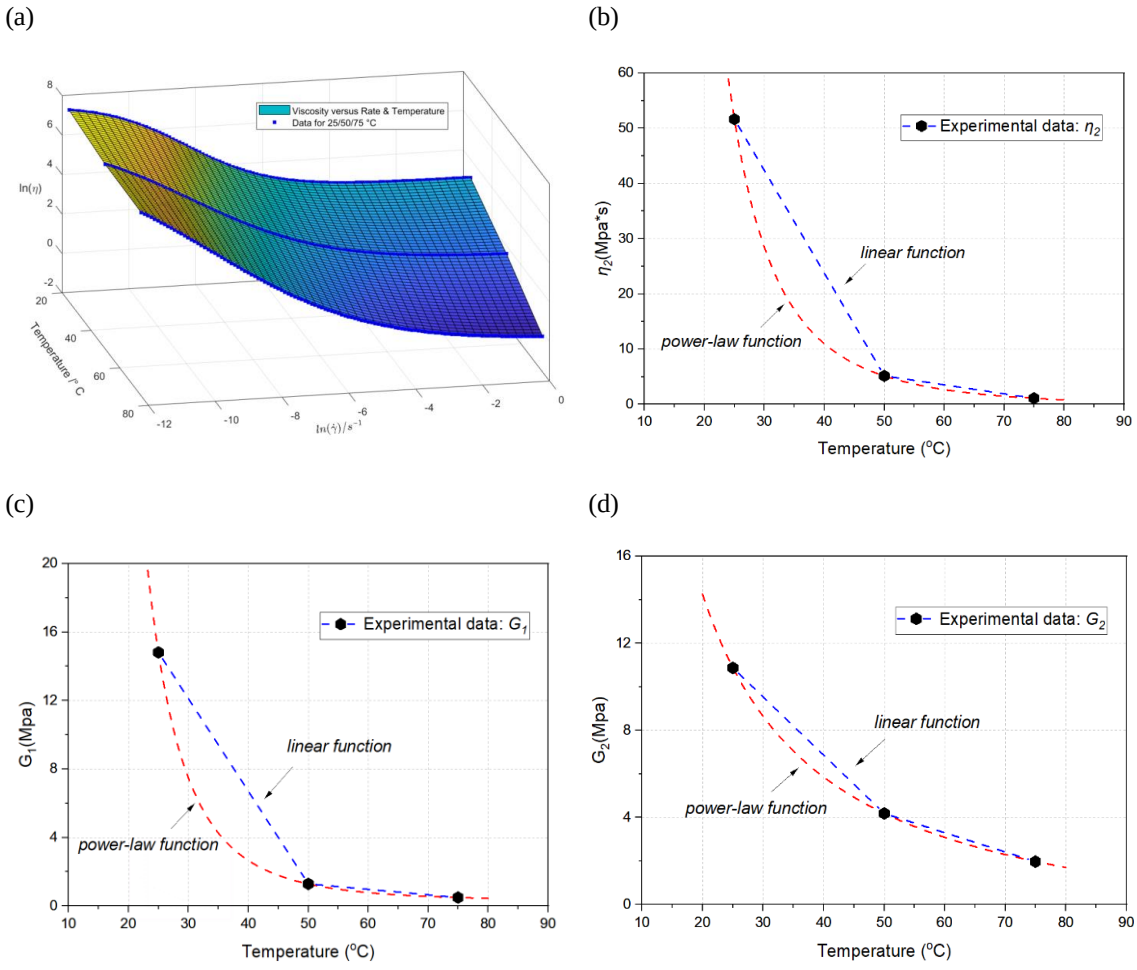

Figure 8 Fit to the experimental data of the evolution of (a) η_1 with temperature and strain rate, (b) η_2, G_1 (c) and G_2 (d) with temperature.

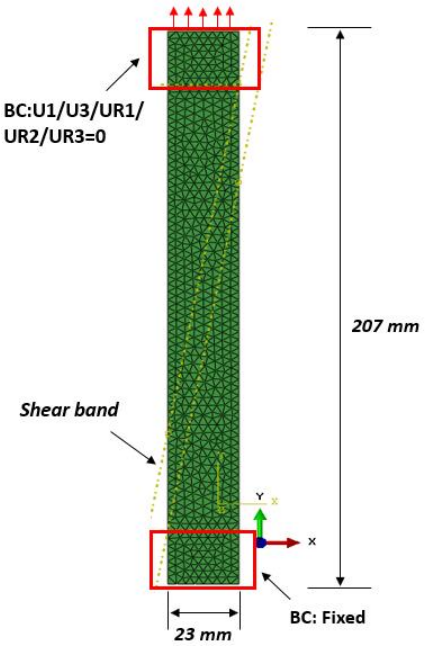

Figure 9 Boundary conditions applied to the FE model of the off-axis tensile test.

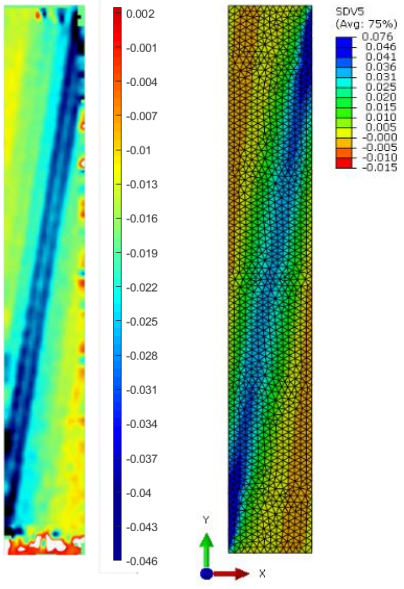

(a) (b)

Figure 10 Shear strain field: (a) DIC results (b) FE predictions.

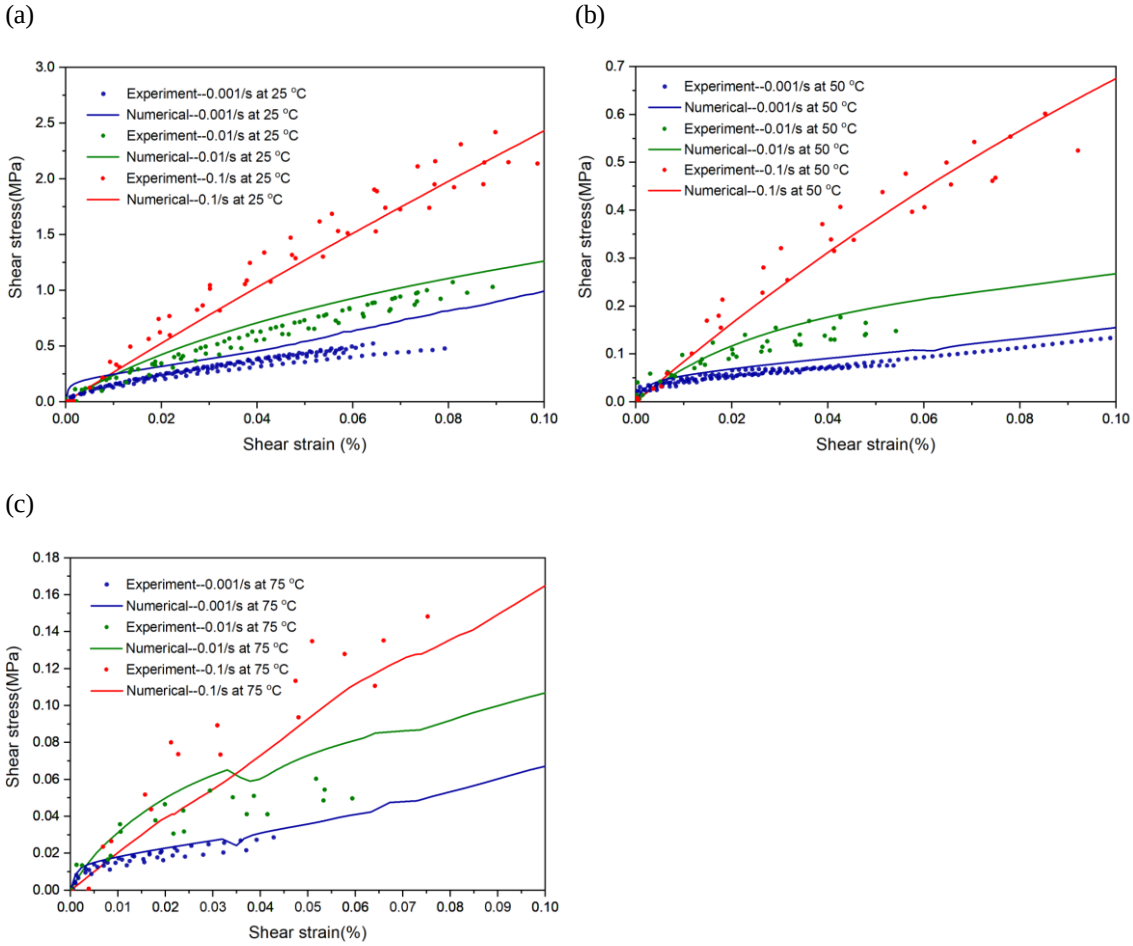

Figure 11 Comparison of experiment and numerical results at 25 °C (a), 50 °C (b) and 75 °C (c) for different test rates.

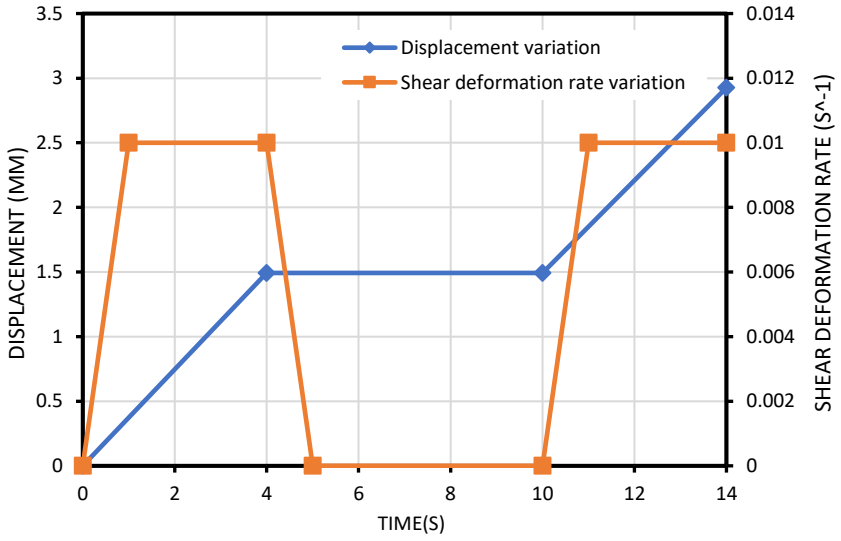

Figure 12 Ramp-dwell test designed for model validation purposes.

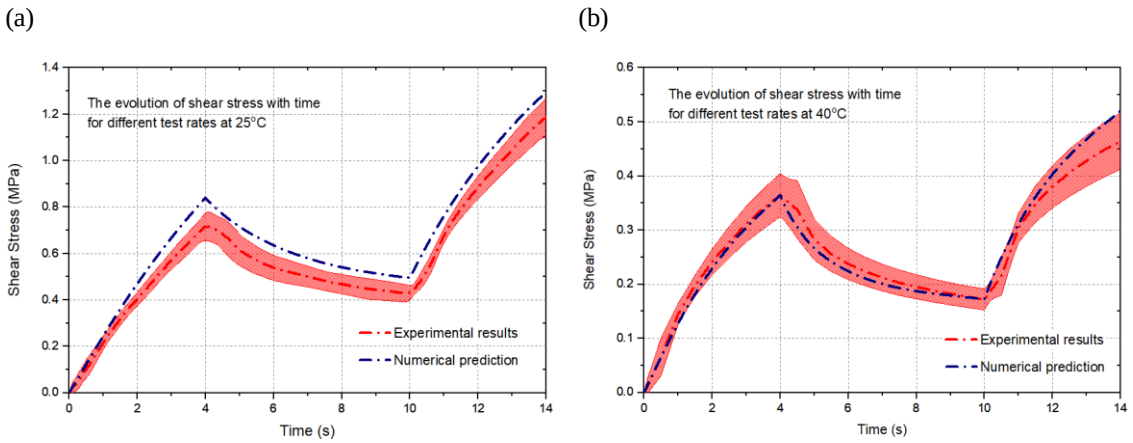

Figure 13 Comparison of experiment and numerical results with different test rates at 25℃ (a) and 40℃ (b).

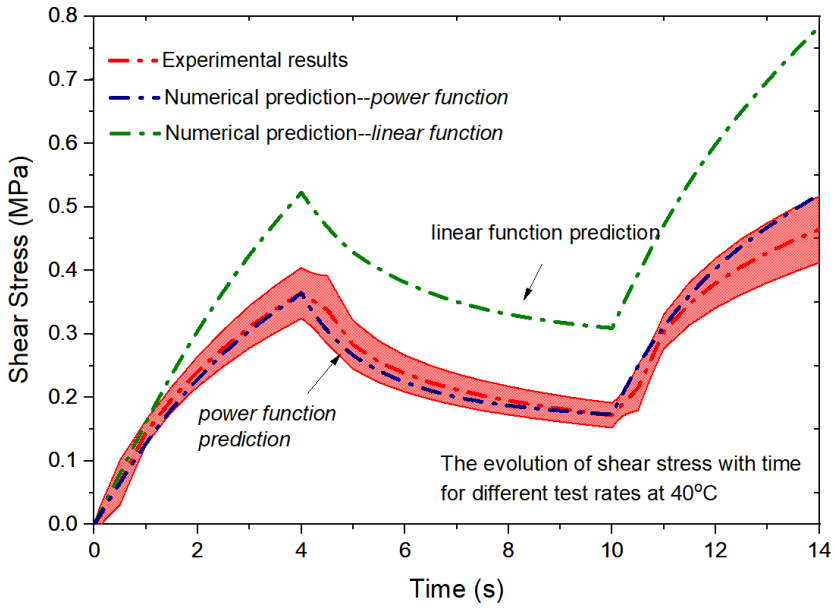

Figure 14 Comparison between power and linear function for terms G_1, G_2 and η_2 across different temperatures.

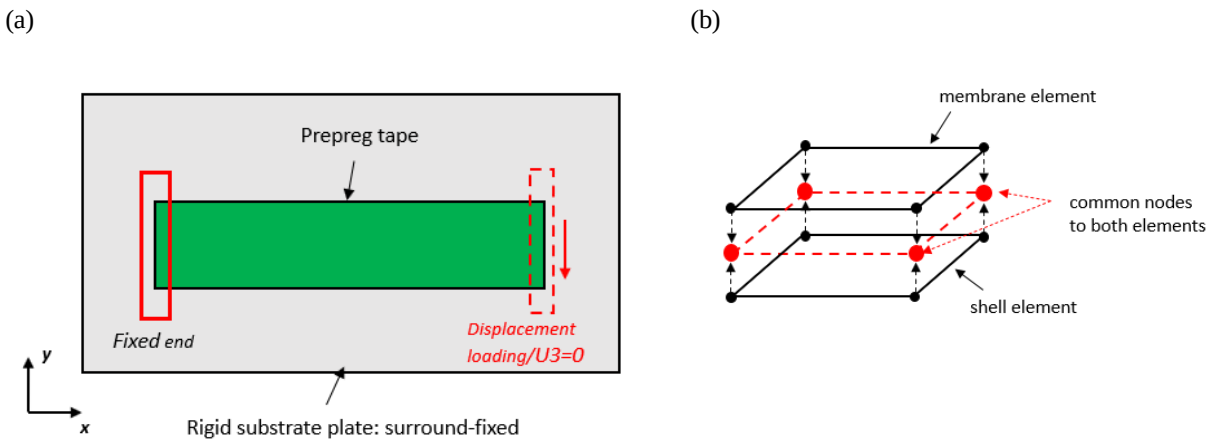

Figure 15 Schematic illustrations of (a) FE bending model and (b) shell-membrane coupling element.

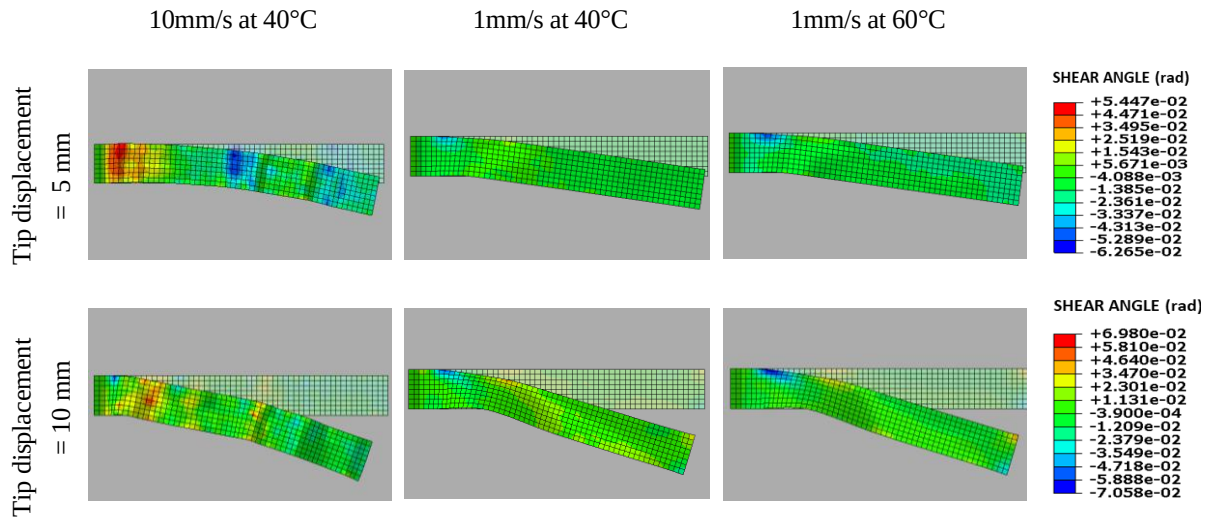

Figure 16 Shear angle distribution in tapes subjected to bending under different temperature and deformation rate conditions.

Tables

Table 1 Rate-dependency of the viscous and elastic term in Equation (2).

$\dot{\gamma}$	**0.001/s**	**0.01/s**	**0.1/s**
η (MPa·s)	136.05	15.5	3.58
G (MPa)	5.51	10.93	21.28

Table 2 Values for η_1 (in log scale) at different rates and temperatures.

Temperature/Rate	**0.001/s**	**0.01/s**	**0.1/s**
25°C	77.375	26.639	26.639
50°C	26.34	7.875	6.656
75°C	6.67	2.08	1.059

Table 3 Summary of the model parameters based on the experiment data.

Temperature/Term	η_2 **(MPa·s)**	G_1 **(MPa)**	G_2 **(MPa)**
25°C	51.648	14.818	10.874
50°C	5.151	1.292	4.183
75°C	1.101	0.495	1.973

Table 4 Values of temperature and rate dependent parameters.

Parameters	$\mathbf{a_{T_i}}$	$\mathbf{b_{T_i}}$	$\mathbf{f_{T_i}}$
25ºC	3.194	7.874	$\tanh(0.52\log(\dot{\gamma}) + 4.135)$
50ºC	1.935	7.817	$\tanh(0.49\ \log(\dot{\gamma}) + 3.94)$
75ºC	-0.095	7.789	$\tanh(0.31\ \log(\dot{\gamma}) + 2.54)$

Table 5 Values of temperature dependent parameters.

Parameters	α_i	β_i	n_i
η_2 **(MPa·s)**	1.703e6	-0.3972	-3.23
G_1 **(MPa)**	3.478e6	0.2825	-3.848
G_2 **(MPa)**	347.7	-2.368	-1.015

Table 6 Comparison of wrinkle severity in tapes deformed at different rate and temperatures.

	10 mm/s at 40°C			1 mm/s at 40°C			1 mm/s at 60°C		
Tip displacement (mm)	Number of wrinkles	Maximum wrinkle wavelength (mm)	Maximum wrinkle amplitude (mm)	Number of wrinkles	Maximum wrinkle wavelength (mm)	Maximum wrinkle amplitude (mm)	Number of wrinkles	Maximum wrinkle wavelength (mm)	Maximum wrinkle amplitude (mm)
5	4	8.83	1.214	1	18.5	2.776	1	19.3	2.579
10	4	10.4	3.182	1	32.1	4.626	1	36.2	4.347